Experimental Evaluation of the Statistical Isotropy of a Reverberation Chamber's Plane-Wave Spectrum

Ryan J. Pirkl, *Member, IEEE*, and Kate A. Remley, *Fellow, IEEE*

***Abstract*—Synthetic-aperture measurements in a loaded reverberation chamber are used to calculate power-angle profiles describing the instantaneous distribution of received power versus azimuth angle-of-arrival. Averaging multiple power-angle profiles leads to estimates of the reverberation chamber's power-angle spectrum. A comparison to simulated power-angle spectra for an ideal reverberation chamber indicates that the loaded reverberation chamber tends to provide a statistically anisotropic plane-wave spectrum. Analysis of the measurements' power-delay-angle profiles suggest that this anisotropy due to both the presence of unstirred multipath components and strong early-time stirred multipath components arising from reflections off of the mode-stirring paddles' planar surfaces. Guidelines are provided for minimizing the effect of a statistically anisotropic plane-wave spectrum, such as the use of additional stirring mechanisms and minimizing the contributions of unstirred multipath components.**

***Index Terms*—Antenna-environment multiple scattering, power-angle profile, power-angle spectrum, power-delay-angle profile, reverberation chamber.**

I. Introduction

THE assumed statistical isotropy of the reverberation chamber's plane-wave spectrum under electrically large measurement conditions (see [1]) has provided insight into the behavior of electric field components, antennas, and other test objects in a reverberation chamber. Examples include spatial correlation functions for field components and antennas [2]–[7], antenna efficiencies [8], [9], absorption cross sections [10], [11], shielding effectiveness [12], and multiple-input multiple-output (MIMO) capacity [13], [14]. However, a direct evaluation of this statistical isotropy assumption has been lacking. To date, the only investigation appearing in the literature is [15], wherein a theoretical justification for a statistically isotropic plane-wave spectrum was made based on the distribution of angles-of-arrival of plane waves in an electromagnetically large and approximately cubic cavity.

Empirical data on the statistical isotropy of a reverberation chamber's plane-wave spectrum is of particular importance to the wireless community, which has been evaluating reverberation chambers as over-the-air test environments [16]–[18]. The long-held assumption of a statistically isotropic plane-wave spectrum leads to expressions for basic performance metrics (e.g., antenna correlation, gain imbalance, capacity [4], [7], [8], [13], [19], [20]) of a multiantenna wireless device in a reverberation chamber. Real-world deviations from a statistically isotropic plane-wave spectrum will affect these basic performance metrics and thereby increase the uncertainty in more complex system-level metrics such as bit-error rate and data throughput.

Here, we evaluate this assumption of a statistically isotropic plane-wave spectrum by way of measurements of the reverberation chamber's power-angle spectra, which describe the average distribution of received power versus azimuth angle-of-arrival for an ensemble of measurement configurations (e.g., multiple paddle positions). A comparison of the measured power-angle spectra to simulated power-angle spectra for an ideal reverberation chamber indicates that a real reverberation chamber's true power-angle spectrum may be angle dependent. This indicates that the plane-wave spectrum in a loaded reverberation chamber may be statistically *anisotropic*. For the loading considered here, the root-mean-square (RMS) ripple factor—the RMS variation of the measured power-angle spectrum, normalized by its mean—was 18–28% and could not be attributed to measurement uncertainty.

Evaluations of the reverberation chamber's power-delay-angle profiles, which describe the instantaneous distribution of received power versus time and azimuth angle-of-arrival for a single measurement configuration (e.g., a single paddle position) indicate that this anisotropy arises primarily due to a combination of unstirred multipath components and strong early-time stirred multipath. As has been shown in prior work [21], [22], a reduction in the chamber's loading is expected to increase the stirred diffuse multipath, and thereby reduce the anisotropy of the chamber's plane-wave spectrum. Additional paddle-averaging may also help to reduce the impact of the strong early-time stirred multipath.

We emphasize that, in this investigation, we evaluate the (an)isotropy of the reverberation chamber's *plane-wave spectrum* by way of the distribution of received power versus angle-of-arrival. This is fundamentally different from [23]–[25], wherein the (an)isotropy of the reverberation chamber's *electric field* (i.e., "polarization imbalance") is evaluated by way of the statistics of the electric field's Cartesian components. It remains to be seen if the statistical isotropy of a chamber's plane-wave spectrum and electric field are complementary or correlated metrics.

Finally, we note that although reverberation chambers are often viewed as resonant cavities in which standing-wave

Manuscript received January 14, 2013; revised July 22, 2013; accepted August 26, 2013. Date of publication November 27, 2013; date of current version May 19, 2014. This work was supported by a National Research Council Postdoctoral Research Associateship. U.S. Government work, not subject to U.S. copyright.

The authors are with the National Institute of Standards and Technology, Electromagnetics Division, RF Fields Group, Boulder, CO 80305 USA (e-mail: rpirkl@gmail.com; kate.remley@nist.gov).

Color versions of one or more of the figures in this paper are available online at http://ieeexplore.ieee.org.

Digital Object Identifier 10.1109/TEMC.2013.2289302

patterns are established, they may also be viewed as scattering environments wherein energy couples between antennas by way of conventional wave propagation mechanisms. This wave-propagation point of view is particularly appropriate for predicting the behavior of wireless devices inside of a reverberation chamber. We adhere to the wave-propagation point of view in our analysis of the reverberation chamber's power-angle profiles and spectra.

We begin by describing the 2-D synthetic-aperture measurements used to sample the reverberation chamber's space-frequency wireless channel in Section II. Section III presents the resulting power-angle profiles, which describe the instantaneous distribution of received power versus azimuth angle-of-arrival. Section IV presents the corresponding power-angle spectra and compares these measured spectra to simulation-based spectra for an ideal, well-stirred reverberation chamber. In Section V, we gain insight into the origins of the chamber's observed anisotropy by way of its power-delay-angle profiles. Implications of a statistically anisotropic plane-wave spectrum and possible mitigation techniques are discussed in Section VI. Concluding remarks and topics for future study are presented in Section VII.

II. Synthetic-Aperture Measurements

Synthetic-aperture measurements, which involve scanning an antenna through space within a static environment, have frequently been used to study the spatial characterisstics of wireless channels [26], [27]. As in [6], [22], and [28], we apply this technique to reverberation chambers. The 2-D (horizontal) planar scanner allows for the synthesis of an aperture with high resolution in azimuth but poor resolution in elevation. Furthermore, 2-D planar scanner measurements cannot be used to determine if an incident plane wave originated from above or below the measurement plane. Despite these shortcomings, an azimuth-only analysis still offers a tremendous amount of insight into the reverberation chamber's plane-wave spectrum, as will be shown.

The setup is illustrated in Fig. 1(a); a to-scale drawing is shown in Fig. 1(b). The measurements were conducted within a 3.60 m $\times$ 4.27 m $\times$ 2.90 m reverberation chamber featuring a pair of physically large rotating paddles. The paddle rotating about a vertical axis swept a cylindrical volume 2.46 m high and 1.00 m in diameter; the paddle rotating about a horizontal axis swept a cylindrical volume 3.3 m long and 1.00 m in diameter. The angular resolution of each stirrer was 0.1°.

A 1-6 GHz vertically polarized biconical antenna served as the "scan" (receive) antenna for the synthetic-aperture measurements. The scan antenna was mounted atop a 2-D positioner capable of scanning a 0.5 m $\times$ 0.5 m planar region. The biconical antenna's radiating element was 0.95 m from the reverberation chamber's floor. The "source" (transmit) antenna was a stationary and horizontally polarized 1–18 GHz dual-ridge-guide horn antenna. The horn was positioned 0.90 m above the chamber's floor and was pointed toward the horizontal mode-stirring paddle. To introduce realistic loading conditions into the chamber and reduce multiple scattering between the scan antenna and the

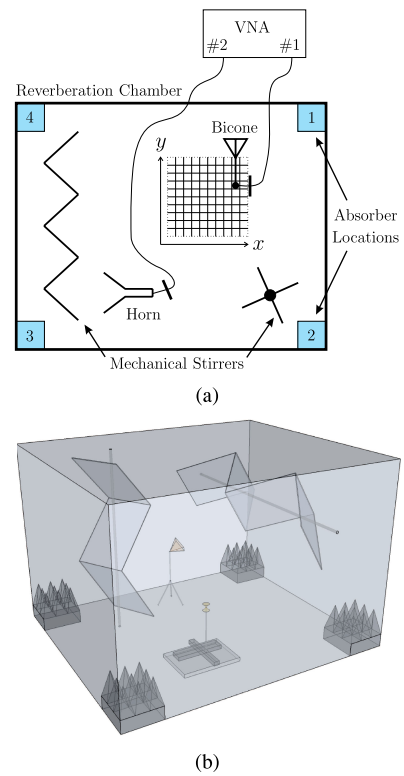

Fig. 1. Synthetic-aperture measurements conducted within the loaded reverberation chamber: (a) top-down diagram and (b) 3-D to-scale drawing. The bicone antenna is aligned with the z-axis.

reverberation chamber, four 0.6 m $\times$ 0.6 m $\times$ 0.6 m three-by-three pyramidal absorber blocks were placed near the chamber's floor corners.

The source and scan antennas were connected to ports #1 and #2, respectively, of a vector network analyzer (VNA), which was calibrated at the antenna ports. The scan antenna was stepped along a 1-cm uniform rectangular grid within the 2-D positioner's 0.5 m $\times$ 0.5 m scan region. The spatial resolution of the 2-D positioner was 6.35 μm. At each observation point, complex S_{21} measurements were recorded from 1 to 6 GHz at 6401 uniformly spaced frequencies. The VNA's intermediate frequency (IF) bandwidth was 100 kHz, and the majority of S_{21} measurements were in the range of $|S_{21}| \in [0, -40]$ dB. For this configuration and range of magnitudes, the manufacturer-specified uncertainties in the magnitude and phase of a single S_{21} measurement were approximately 0.2 dB and 1°, respectively.

The synthetic-aperture measurements were repeated for nine unique sets of paddle orientations. Using wireless channel terminology, we denote the S_{21} data as the channel's transfer function $h^{(n)}(f, \mathbf{r})$, where f is the measurement frequency, $\mathbf{r} = (x, y)$ is the scan antenna's position in a 2-D space, and $n = 1, \ldots, 9$ denotes the nine unique paddle orientations.

III. Power-Angle Profiles

From the 2-D spatial wireless channel measurements, we calculate the reverberation chamber set-up's corresponding

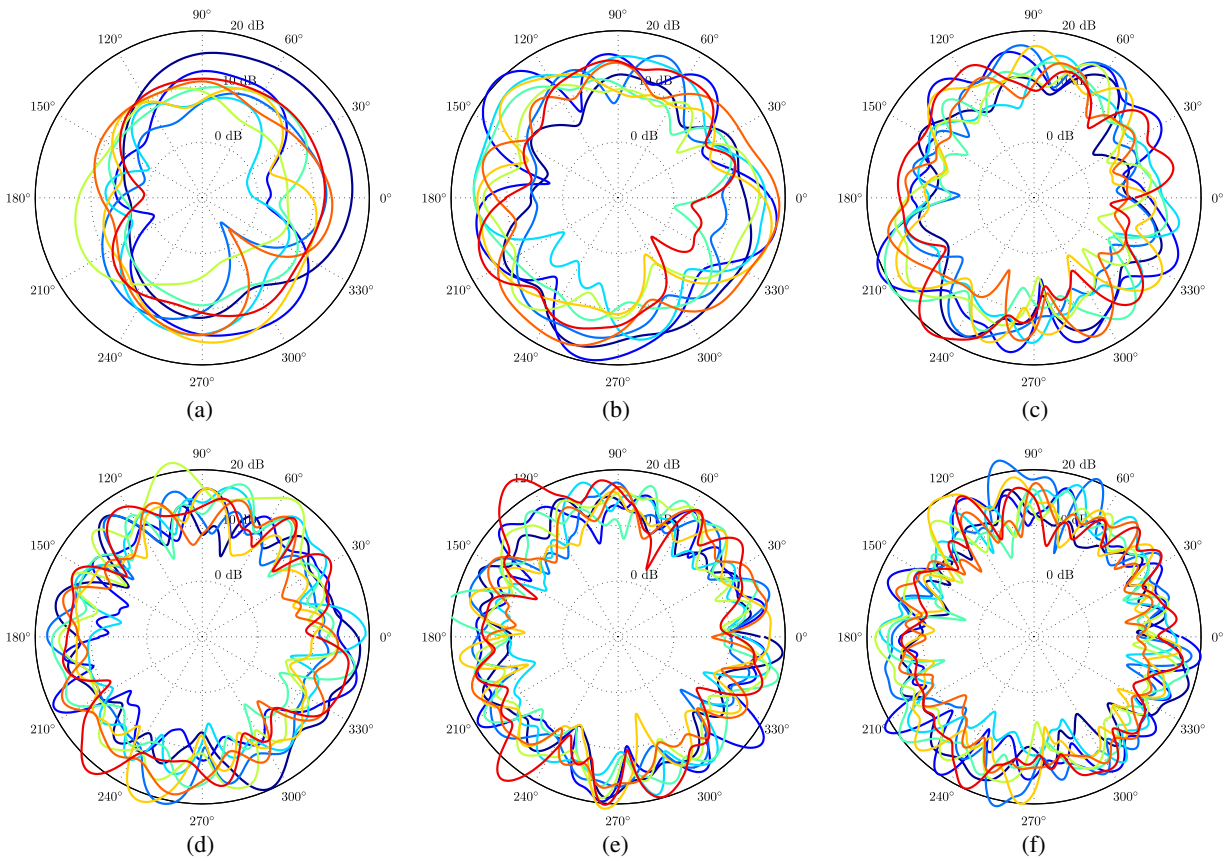

Fig. 2. Power-angle profiles measured at different paddle positions. Each plot shows results for a different frequency. The nine traces in each plot correspond to power-angle profiles for the nine paddle orientations. The data are normalized such that 0 dB corresponds to the measurement's noise floor. (a) 1 GHz. (b) 2 GHz. (c) 3 GHz. (d) 4 GHz. (e) 5 GHz. (f) 6 GHz.

power-angle profiles, which describe the instantaneous distribution of received power versus azimuth angle-of-arrival. We first calculate the 2-D spatial wireless channel's power-wavevector profile $p^{(n)}(f, \mathbf{k})$, which is the magnitude-square of the 2-D spatial Fourier transform of a single channel measurement (cf. [29]):

$$p^{(n)}(f, \mathbf{k}) = \left| \int h^{(n)}(f, \mathbf{r}) e^{j\mathbf{k}\cdot\mathbf{r}}\, d\mathbf{r} \right|^2 \tag{1}$$

where $\mathbf{k}$ denotes the 2-D wavevector and the integration is over 2-D position $\mathbf{r} = (x, y)$. To minimize aperture sidelobes, a rotationally symmetric 2-D Hamming window was applied along the 2-D spatial dimension of $h^{(n)}(f, \mathbf{r})$ prior to (1)'s Fourier transform. We express $\mathbf{k}$ in cylindrical coordinates as $\mathbf{k} = (k\cos\beta, k\sin\beta)$, where k is the wavenumber and β is the direction-of-propagation such that the power-wavevector profile is denoted as $p^{(n)}(f, k, \beta)$. We assume that only homogeneous plane waves contribute to the observed channel due to the large electrical separation between sources, scatterers, and antennas. Thus, we define the corresponding power-angle profile $p^{(n)}(f, \phi)$ as

$$p^{(n)}(f, \phi) = \int_0^{k_0} p^{(n)}(f, k, \phi + \pi) k\, dk \tag{2}$$

where k_0 is the free-space wavenumber and direction-of-propagation β has been mapped to azimuth angle-of-arrival ϕ. Physically, the integration with respect to wavenumber k amounts to an integration with respect to the elevation angle-of-arrival. Thereby, $p^{(n)}(f, \phi)$ is the received power at a given azimuth angle ϕ due to multipath components arriving from both on- and off-the-horizon.

Fig. 2 presents the measured power-angle profiles for the nine unique paddle orientations at six different frequencies. For additional insight, Fig. 3 presents the power-angle profiles for nine closely spaced frequencies at each of the six center frequencies considered in Fig. 2. The nine power-angle profiles in each plot were calculated at coherence bandwidth intervals B_c from within a $9B_c$ bandwidth that was nominally[1] centered about each of the "center frequencies" used in Fig. 2. This frequency spacing provides uncorrelated frequency samples that, when averaged, will reduce the measurement uncertainty. Here, $B_c = 3.6$ MHz as determined from the full-width at half-maximum of the wireless channel's frequency-domain autocovariance [30], [31]. This corresponds to quality factors ranging from approximately 300 to 1600 at 1 GHz and 6 GHz, respectively.

The power-angle profiles in Figs. 2–3 have been normalized by the noise power spectral density such that the individual power-angle profiles may be interpreted as received power with respect to the measurement noise floor. Hence, 0 dB corresponds

[1]For 1 and 6 GHz, these "center frequencies" correspond to lower and upper limits, respectively, of the $9B_c$ bandwidth.

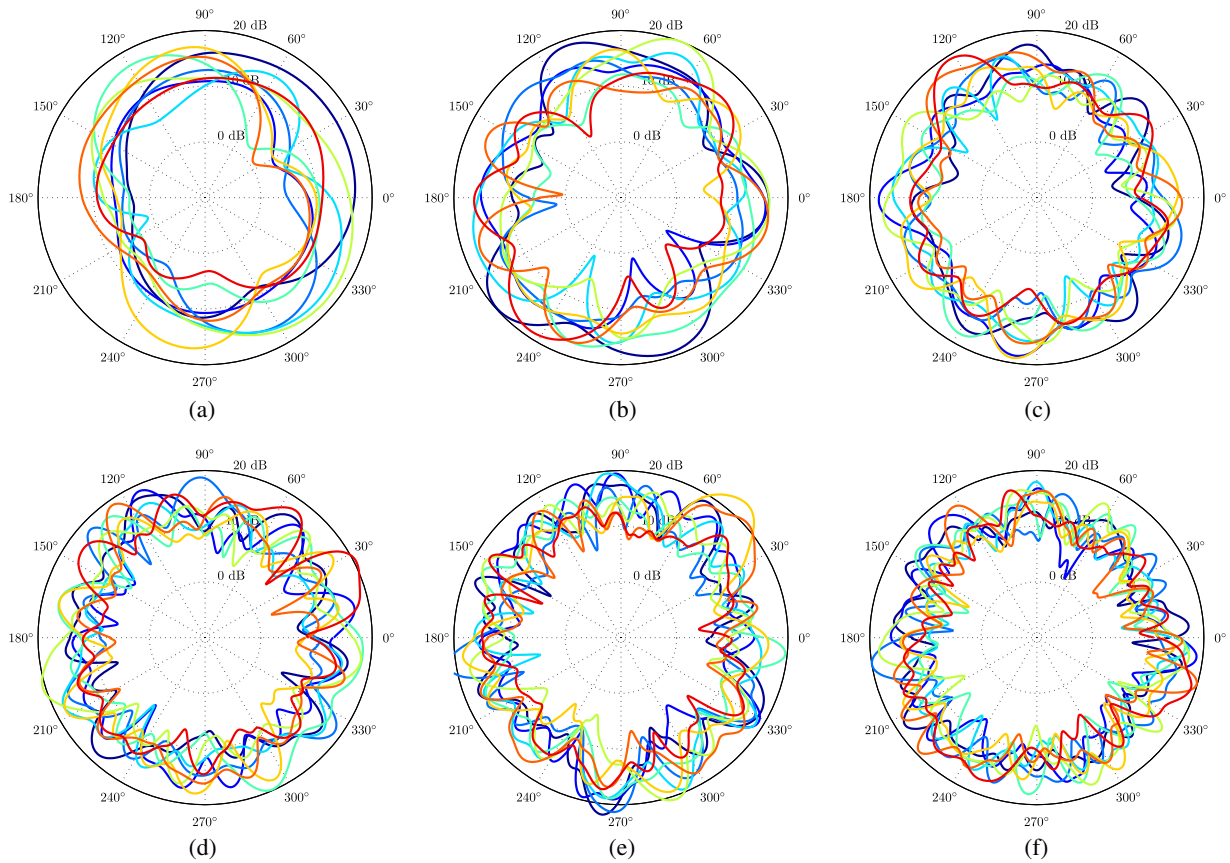

Fig. 3. Power-angle profiles measured at different frequencies within a $9B_c$ bandwidth. Each plot shows results for a different center frequency. The nine traces in each plot correspond to power-angle profiles for nine frequencies at approximately B_c intervals. All of the plots correspond to the same paddle configuration. The data are normalized such that 0 dB corresponds to the measurement's noise floor. (a) 1 GHz. (b) 2 GHz. (c) 3 GHz. (d) 4 GHz. (e) 5 GHz. (f) 6 GHz.

TABLE I
MEASUREMENT SNR

Frequency	1 GHz	2 GHz	3 GHz	4 GHz	5 GHz	6 GHz
SNR	11 dB	13 dB	13 dB	14 dB	15 dB	14 dB

TABLE II
UNCERTAINTY IN NOISE-FLOOR-NORMALIZED QUANTITIES

$\hat{p}/\hat{n}$	15 dB	10 dB	5 dB	0 dB
Power Profiles	$+0.1$ dB -0.1 dB	$+0.5$ dB -0.5 dB	$+1.7$ dB -2.7 dB	$+\infty$ dB $-\infty$ dB
Power Spectra	$+0.5$ dB -0.5 dB	$+0.6$ dB -0.7 dB	$+1.7$ dB -2.8 dB	$+\infty$ dB $-\infty$ dB

to the noise floor of each plot. The measurement noise was attributed to a combination of the VNA's receiver noise and wireless channel perturbations due to antenna-chamber multiple scattering, whereby the nonstationary scan antenna effectively behaves like a mode-stirring paddle [6], [28]. Appendices A and B give an overview of the nontrivial procedure for estimating this noise. Table I presents the measurement's signal-to-noise ratio (SNR) at each center frequency. Uncertainties for the noise-floor-normalized quantities presented throughout this paper are given in Table II, where $\hat{p}/\hat{n}$ denotes a generic noise-floor-normalized quantity. The process for calculating Table II's uncertainties is described in Appendix C. The first two rows of uncertainties apply to the power-angle and power-delay-angle profiles presented here and in Section V; the last two rows apply to the power-angle spectra presented in Section IV.

Comparing the sets of power-angle profiles in Figs. 2–3, there is no obvious structure that is consistent across frequencies or paddle orientations. The angle-dependent variation is expected because these are "instantaneous" power-angle profiles for individual frequencies and stirrer positions rather than aggregate power-angle spectra. The increased rate of angle-dependent variations at higher frequencies is due to the improved angular resolution of the synthetic-aperture array at high frequencies. The joint angle-frequency selectivity of the power-angle profiles presented in Fig. 3 indicates that within a given angular sector corresponding to the aperture's beamwidth, there are a large number of incident multipath components with different times-of-arrival. Thereby, the reverberation chamber provides a multipath-rich scattering environment. In the following section, we assess whether or not an ensemble of these multipath-rich wireless channels emulates a statistically isotropic scattering environment characterized by a statistically isotropic plane-wave spectrum.

IV. POWER-ANGLE SPECTRA

An estimate of the reverberation chamber's power-angle spectrum, denoted $\hat{\bar{p}}(f, \phi)$, is given by the ensemble average of a set

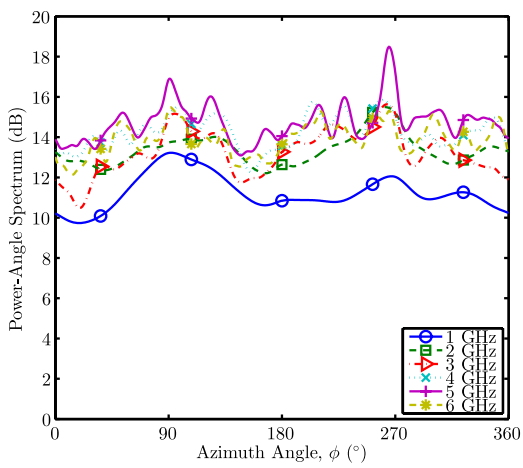

Fig. 4. Power-angle spectra as a function of azimuth angle-of-arrival calculated by averaging the power-angle profiles over the nine paddle orientations and a $9B_c$ bandwidth about each center frequency. The data are normalized such that 0 dB corresponds to the measurement's noise floor.

of power-angle profiles:

$$\hat{\bar{p}}(f,\phi) = \langle p^{(n)}(f,\phi)\rangle_n \tag{3}$$

where $\langle\cdot\rangle_n$ denotes an ensemble average with respect to paddle orientations. Thereby, $\hat{\bar{p}}(f,\phi)$ describes the expected distribution of received power as a function of azimuth angle at a given frequency. Due to the small number of paddle positions used in our measurement dataset, we extend (3) by also averaging $\hat{\bar{p}}(f,\phi)$ across nine B_c-spaced frequencies for a given "center frequency." This small amount of additional frequency-averaging leads to a significant reduction in the uncertainty in our estimate.

Fig. 4 compares $\hat{\bar{p}}(\phi)$ at the different center frequencies considered in Figs. 2–3. For an ideal reverberation chamber, the true power-angle spectrum is expected to be invariant with respect to azimuth angle ϕ. Based on the uncertainties in Table II, the ripple, or variance in the estimated power-angle spectra with respect to the mean, is presented in Fig. 4 is statistically significant and indicates that the loaded reverberation chamber's plane-wave spectrum is statistically anisotropic.

As an auxiliary confirmation and to gauge the extent of the anisotropy, we compare the ripple in the measurement-based power-angle spectra to the ripple in corresponding simulation-based power-angle spectra for an ideal and well-stirred reverberation chamber. For our simulations, we use the computationally efficient stochastic plane-wave spectrum model described in [32]. For each center frequency, the stochastic plane-wave spectrum was sampled by a vertically polarized infinitesimal dipole on a 1-cm uniform rectangular grid spanning a 0.5 m $\times$ 0.5 m region in the xy plane. This mimics the synthetic-aperture measurements conducted with the biconical scan antenna. Additive white Gaussian noise was used to match the simulations' SNRs to those of the measurements, as given in Table I. Sets of 81 simulated synthetic-aperture measurements were processed with the same method that was applied to the actual measurements so as to generate comparable simulation-based power-angle spectra for the ideal reverberation chamber.

TABLE III
POWER-ANGLE SPECTRUM RIPPLE FACTOR (%)

Frequency	Measurement		Simulation		
	Full	Stirred	Mean	5th Percentile	95th Percentile
1 GHz	22	9	8	5	13
2 GHz	20	12	9	6	12
3 GHz	30	18	8	6	11
4 GHz	17	16	8	6	10
5 GHz	28	17	8	6	9
6 GHz	18	17	7	6	9

Table III compares the RMS ripple factor for the measured and simulated power-angle spectra. The RMS ripple factor was calculated as the RMS of the ripple normalized by the mean. For the measurement-based ripple factors, the "Full" column corresponds to the ripple factors of power-angle spectra presented in Fig. 4. The "Stirred" column corresponds to the ripple factors of power-angle spectra calculated from $h^{(n)}(f,\mathbf{r}) - \langle h^{(n)}(f,\mathbf{r})\rangle_n$; that is, after the unstirred wireless channel's contribution ($\langle h^{(n)}(f,\mathbf{r})\rangle_n$) was removed from the measurements. This provides an estimate of into how much of the loaded chamber's statistical anisotropy is due to the presence of unstirred multipath components. For the simulation-based ripple factors, we consider three statistics: the mean ripple factor, and the 5th and 95th percentile of the simulated data's cumulative distribution function. The mean corresponds to the nominal ripple factor for a plane-wave spectrum measured in an ideal reverberation chamber; the percentiles provide lower and upper bounds on expected ripple factors.

At all frequencies, the "Full" measured power-angle spectra's ripple factor is larger than 95% of the simulation-based ripple factors. This indicates that the angle-dependent variations of the measured power-angle spectra presented in Fig. 4 are much larger than would be expected for an ideal reverberation chamber. This further confirms that Fig. 4's measured power-angle spectra are not representative of a statistically isotropic plane-wave spectrum. The "Stirred" power-angle spectra exhibit smaller ripple factors than the "Full" spectra. This indicates that a considerable portion of the loaded reverberation chamber's statistical plane-wave anisotropy is due to the presence of unstirred multipath components—when the unstirred wireless channel is removed, the ripple factor is reduced.

Note that at 1 and 2 GHz, the "Stirred" power-angle spectra's ripple factors fall within the lower (5th percentile) and upper (95th percentile) bounds of the simulation-based ripple factors, whereas above these frequencies, the ripple factor continues to exceed the simulations' 95th percentiles. This weak frequency dependence is expected to be largely due to the frequency-dependent directivity of the 2-D synthetic aperture. At lower frequencies, the synthetic aperture is electromagnetically smaller and, thus, has a lower directivity (i.e., a lower angular resolution). This lower directivity leads to an implicit angular smoothing of power versus angle-of-arrival that may mask angle-dependent variations in the reverberation chamber's true power-angle spectrum.

V. Power-Delay-Angle Profiles

For further insight into the observed statistical anisotropy of the reverberation chamber's plane-wave spectrum, we examine the power-delay-angle profile $p^{(n)}(\tau, \phi)$ measured for each paddle configuration. The power-delay-angle profile describes the instantaneous distribution of received power with respect to time-of-arrival (i.e., delay) τ and azimuth angle-of-arrival ϕ. It may be calculated from each measurement's 2-D space- and frequency-dependent delay-wavevector profile $p^{(n)}(\tau, \mathbf{k})$, which is given by the magnitude squared of the channel's frequency and 2-D spatial Fourier transform (cf. [29]):

$$p^{(n)}(\tau, \mathbf{k}) = \left| \iint h^{(n)}(f, \mathbf{r}) e^{j2\pi\tau f} e^{j\mathbf{k}\cdot\mathbf{r}} \, df \, d\mathbf{r} \right|^2. \quad (4)$$

To minimize aperture and delay-domain sidelobes, a rotationally symmetric 2-D Hamming window and a 1-D Hamming window were applied along the 2-D spatial dimension and 1-D frequency dimension of $h^{(n)}(f, \mathbf{r})$ prior to (4)'s Fourier transforms. Analogous to the definition of the power-angle profile in (2), we define the power delay-angle profile as

$$p^{(n)}(\tau, \phi) = \int_0^\infty p^{(n)}(\tau, k, \phi + \pi) k \, dk. \quad (5)$$

Fig. 5 presents noise-floor-normalized power-delay-angle profiles for a subset of the paddle orientations. Each "pulse" in the power-delay-angle profile indicates the azimuth angle, delay, and relative power of one or more multipath components incident on the scan region.[2] Comparing the different power-delay-angle profiles, we observe numerous strong pulses within an otherwise noise-like distribution of power. This noise-like power corresponds to diffuse stirred multipath associated with the statistically isotropic plane-wave spectrum of an ideal, well-stirred reverberation chamber.

Fig. 6 presents power-delay-angle profiles calculated from the stirred channels, as given by $h^{(n)}(f, \mathbf{r}) - \langle h^{(n)}(f, \mathbf{r}) \rangle_n$ (i.e., after removal of the unstirred channel); the power-delay-angle profile calculated from the unstirred channel as given by $\langle h^{(n)}(f, \mathbf{r}) \rangle_n$ (see [22]) is presented in Fig. 7. The tone scales of Figs. 6 and 7 were chosen to facilitate comparisons with Fig. 5.

The majority of the strong multipath components in Fig. 5 appear in the Fig. 7's unstirred channel power-delay-angle profile and are absent in Fig. 6's stirred channel power-delay-angle profiles. However, a sparse set of statistically significant, early-time, and paddle-dependent (i.e., stirred) pulses remain. Following the terminology and decompositions used in [29], we draw a distinction between these strong paddle-dependent pulses, which we refer to as stirred *specular* multipath, and the weaker, more noise-like stirred *diffuse* multipath associated with an ideal and well-stirred reverberation chamber. The "specular" and "diffuse" descriptors are based entirely on the relative power of multipath components and are independent of a multipath component's underlying propagation mechanisms.

[2]Due to the finite spatial and temporal resolution of the measurements, as well as the absence of elevation angle-of-arrival information, it is impossible to determine whether a given pulse corresponds to a single multipath component or a tightly grouped cluster of multipath components with similar time- and angle-of-arrival characteristics.

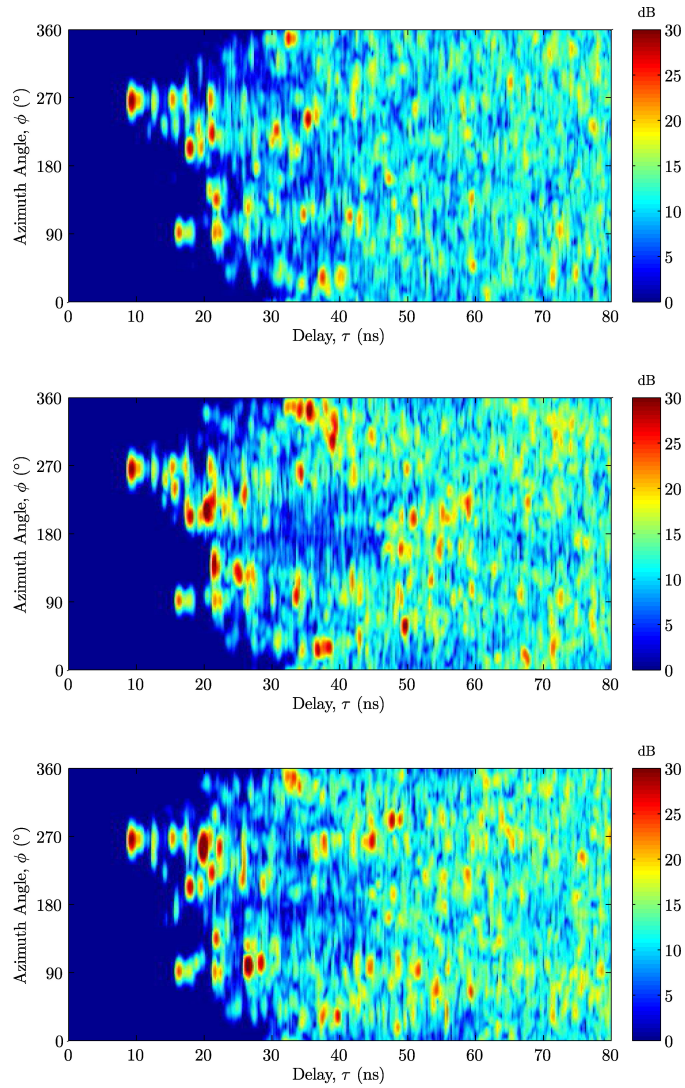

Fig. 5. Power-delay-angle profiles for three different paddle orientations. The data are normalized such that 0 dB corresponds to the power-delay-angle profile's noise floor.

Whereas the unstirred multipath components are well predicted by image theory for a rectangular cavity [22], these stirred specular multipath components are not. Thus, the propagation paths corresponding to the stirred specular multipath components include some form of interaction with the chamber's paddles. Stirred multipath components arising due to diffraction off the paddles' edges may be expected to exhibit relatively consistent times- and angles-of-arrival, albeit varying amplitudes and phases, for different paddle orientations. This is because, whereas the orientation of the paddles (i.e., the scatterers) is changing, the geometric center of the scatterer is fixed. However, from inspection of Fig. 6, we observe that the stirred specular multipath components do not have consistent times- and angles-of-arrival across different paddle orientations. Based on these considerations, we hypothesize that stirred specular multipath components are due to ray-like specular reflections off of the planar surfaces of our physically large "Z"- and "W"-shaped paddles. Additional rotation of the paddles would drastically

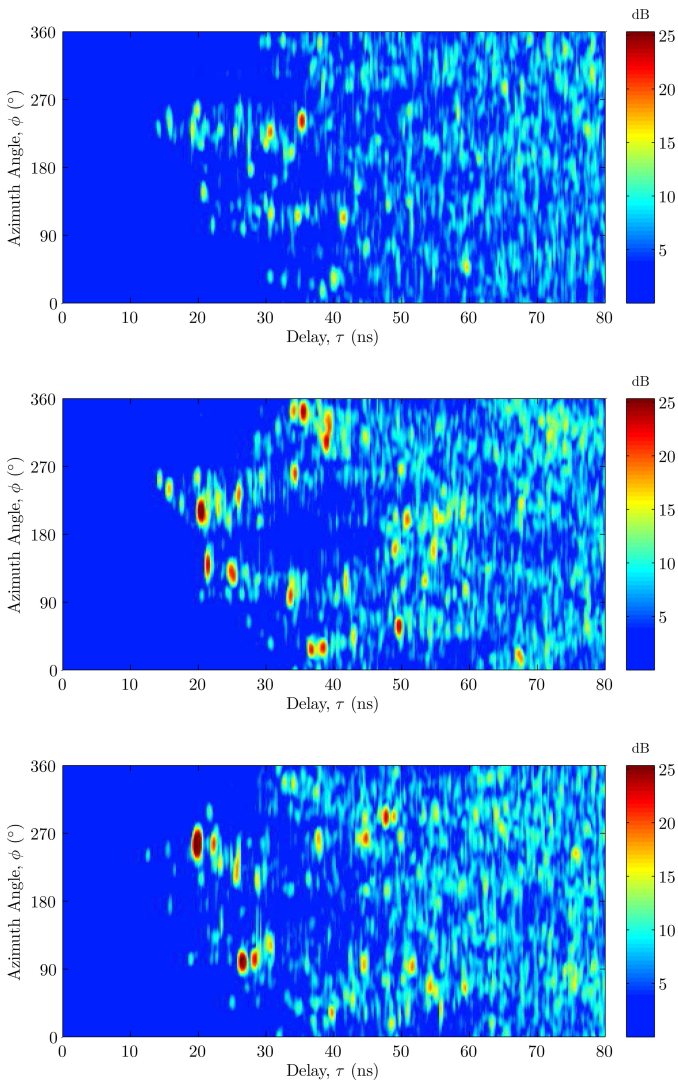

Fig. 6. Stirred power-delay-angle profiles for the same three paddle orientations as considered in Fig. 5. The data are normalized such that 0 dB corresponds to the power-delay-angle profile's noise floor.

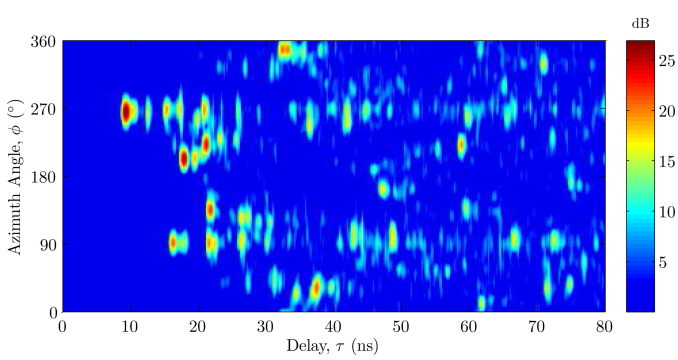

Fig. 7. Unstirred power-delay-angle profile for the measurements. The data are normalized such that 0 dB corresponds to the power-delay-angle profile's noise floor.

alter these ray-like propagation paths and result in the observed seemingly erratic presence/absence of the stirred specular multipath components at different paddle orientations.

VI. Discussion

The results and analysis presented in Sections IV–V indicate that real-world reverberations chamber may exhibit a statistically anisotropic plane-wave spectrum in the presence of unstirred multipath components and/or stirred specular multipath components. Importantly, this does not imply that the assumption of a statistically isotropic plane-wave spectrum is useless or categorically invalid. In fact, the power-angle spectra presented in Fig. 4 indicate that assuming an angle-invariant power-angle spectrum is a reasonable first approximation for reverberation chambers.

This first approximation is expected to be especially applicable for measurements with low-directivity antennas, because they provide an intrinsic angular smoothing of the reverberation chamber's true power-angle spectrum and are thus relatively insensitive to orientation. Contrast this with measurements that use high-directivity antennas, which could be pointed in directions of maximum (or minimum) incident power and thereby are expected to be more sensitive to variations in an environment's power-angle spectrum. This sensitivity to directivity was observed in the frequency/directivity-dependent ripple factors for the "Stirred" power-angle spectra, as discussed in Section IV.

Fine tuning of the measurement configuration may reduce the variations in the reverberation chamber's power-angle spectra and bring it more closely in alignment with an ideal reverberation chamber. Techniques for reducing the reverberation chamber's Rician K-factor [21], [22] (e.g., adjusting the position and orientation of the transmitting antennas, reducing the chamber's loading, using many larger mechanical stirrers, use of chamber walls with irregular surfaces, etc.) will reduce the impact of the unstirred multipath components. Assuming the stirred specular components are due to specular reflections off of the paddles, as hypothesized here, their impact may be mitigated by use of paddle designs featuring electromagnetically rough diffusors and/or nonplanar surfaces (e.g., [33]). The use of more unique paddle orientations to attain an ensemble average should also help to "average out" the stirred specular multipath components and thereby mitigate their effect. Supplemental stirring techniques that change the orientation of the antenna(s) (e.g, position, platform, and source stirring [34]–[36]) are expected to improve the *perceived* statistical isotropy of the reverberation chamber, because they synthetically distribute the angle-of-arrival of multipath components. This was illustrated in [7] for the case of an undermoded reverberation chamber.

This sudy has confirmed that, depending on the measurement configuration, the reverberation chamber's plane-wave spectrum may be statistically anisotropic. However, the critical task of relating this anisotropy to uncertainty in measured quantities remains unaddressed. We also note that, given the numerous instances of good agreement between experimental results and theoretical results developed under the assumption of a statistically isotropic plane-wave spectrum (e.g., [2], [5], [6], [8], [9], [11]–[14]), the uncertainty due to anisotropy may prove to be negligible for many measurement applications. For measurements of nonlinear figures of merit such as bit-error rate or data throughput, additional models may be needed for a complete uncertainty analysis.

Finally, we emphasize that the results presented here were for a single reverberation chamber with a specific measurement setup. The extent to which these results are representative of measurements in other chambers remains to be seen. Different chamber geometries, stirrer configurations, loading conditions, and even transmit antennas may result in a test environment with a true statistically isotropic plane-wave spectrum.

VII. Conclusion

The assumption that a reverberation chamber provides a statistically isotropic plane-wave spectrum has led to a tremendous amount of insight into how fields, antennas, and other test objects behave in a reverberation chamber. By way of the first-ever direct measurements of a reverberation chamber's plane-wave spectrum, we have shown that this assumption is a reasonable first approximation, but it may be erroneous in the presence of unstirred multipath components and/or stirred specular multipath components.

Depending on the application, we expect that refinements to a given measurement configuration, such as reducing the loading and adding diffusors to the stirrers' surfaces, should enable most reverberation chambers to realize a satisfactory statistically isotropic plane-wave spectrum. For scenarios where one cannot further tweak the measurement configuration (e.g., where loading is necessary to attain a specific coherence bandwidth), it may be important to account for the additional measurement uncertainty due to the statistical anisotropy of a chamber's plane-wave spectrum. However, the challenging task of relating this anisotropy to measurement uncertainty remains and is a topic of future study.

It would be insightful to repeat the measurements with a lighter loading condition (i.e., fewer RF absorbers). This is expected to reveal a more statistically isotropic plane-wave spectrum due to the increase in diffuse stirred power. However, the uncertainty in the synthetic-aperture measurements would also increase due to the expected increase in antenna-chamber multiple scattering [6], [28]. Repeating the measurements with a 3-D synthetic-aperture measurement would also be desirable. This would allow the power-angle spectrum to be characterized in both azimuth and elevation so as to yield a more complete evaluation of the plane-wave spectrum's statistical (an)isotropy. A 3-D synthetic-aperture measurement would also allow for further investigation into the origin of the stirred specular multipath components.

Appendix A
Noise Power Spectral Density

From the analysis presented in [6] and [28], we expect that the uncertainty in quantities derived from synthetic-aperture measurements will be dominated by antenna-chamber multiple scattering, which effectively raises the noise floor of the measurements. This raised noise floor impacts the noise floor of associated power spectra and power profiles. To determine the noise floor of these power spectra and power profiles, we consider a simple statistical model of the measured wireless channel. Note that assumptions made here apply only to the noise floor estimation and, thereby, the normalization of the quantities presented in Figs. 2–7.

A. Measurement Model

We describe the nth measured channel as a superposition of three terms:

$$h^{(n)}(f,\mathbf{r}) = h_0^{(n)}(f,\mathbf{r}) + h_{\text{scatt}}^{(n)}(f,\mathbf{r}) + h_{\text{noise}}^{(n)}(f,\mathbf{r}) \tag{6}$$

where $h_0^{(n)}(f,\mathbf{r})$ is the "true" channel as would be measured with a fictitious nonscattering antenna, $h_{\text{scatt}}^{(n)}(f,\mathbf{r})$ is the perturbation due to antenna-chamber multiple scattering, and $h_{\text{noise}}^{(n)}(f,\mathbf{r})$ is the perturbation due to additive white Gaussian noise (AWGN) at the receiver. We model these three terms as independent, zero-mean, and wide-sense stationary stochastic processes.

A joint space-frequency Fourier transform of $h^{(n)}(f,\mathbf{r})$ yields a delay-wavevector representation of the measured channel:

$$H^{(n)}(\tau,\mathbf{k}) = H_0^{(n)}(\tau,\mathbf{k}) + H_{\text{scatt}}^{(n)}(\tau,\mathbf{k}) + H_{\text{noise}}^{(n)}(\tau,\mathbf{k}). \tag{7}$$

The power-delay-wavevector spectrum of the channel is given by

$$p(\tau,\mathbf{k}) = \mathrm{E}\{|H^{(n)}(\tau,\mathbf{k})|^2\}. \tag{8}$$

From inspection of (8), we note that $p(\tau,\mathbf{k})$ is also the variance of the zero-mean stochastic process $H^{(n)}(\tau,\mathbf{k})$. In (8), $\mathrm{E}\{\cdot\}$ denotes the expectation operator. Combining (7), (8), and our assumptions about the terms in (6), we have

$$p(\tau,\mathbf{k}) = p_0(\tau,\mathbf{k}) + p_{\text{scatt}}(\tau,\mathbf{k}) + p_{\text{noise}}(\tau,\mathbf{k}) \tag{9}$$

where $p_0(\tau,\mathbf{k}), p_{\text{scatt}}(\tau,\mathbf{k})$, and $p_{\text{noise}}(\tau,\mathbf{k})$ are the power-delay-wavector spectra (i.e., variances) of the three contributing terms in (6).

Integrating each of the quantities in (9) with respect to the wavenumber k and equating $\phi = -\beta$ as in (2) yields the associated power-delay-angle spectra:

$$p(\tau,\phi) = p_0(\tau,\phi) + p_{\text{scatt}}(\tau,\phi) + p_{\text{noise}}(\tau,\phi). \tag{10}$$

These power-delay-angle spectra satisfy the following set of equalities:

$$\int_0^{2\pi}\int_0^T p_0(\tau,\phi)\,d\phi d\tau = P_0 \tag{11}$$

$$\int_0^{2\pi}\int_0^T p_{\text{scatt}}(\tau,\phi)\,d\phi d\tau = P_{\text{scatt}} \tag{12}$$

$$\int_0^{2\pi}\int_0^T p_{\text{noise}}(\tau,\phi)\,d\phi d\tau = P_{\text{noise}} \tag{13}$$

$$\int_0^{2\pi}\int_0^T p(\tau,\phi)\,d\phi d\tau = P_0 + P_{\text{scatt}} + P_{\text{noise}}. \tag{14}$$

Here, $\tau \in [0,T)$, with $T = \frac{1}{\Delta f}$ being the maximum delay that may be resolved unambiguously for VNA measurements with a frequency spacing of Δf. P_0, P_{scatt}, and P_{noise} are the total power in the "true" channel, the multiple scattering perturbation, and the VNA noise perturbation, respectively. The total power

terms may be determined by way of an empirical estimate of the spatial autocovariance of S_{21} as described in Appendix B.

We assume that the delay and angle dependences of these spectra are separable. Furthermore, we assume that the power is uniformly distributed in azimuth. This is appropriate for spatially white noise (i.e., AWGN due to the VNA) as well as power received in an ideal and well-stirred reverberation chamber. This is also a reasonable first approximation for the antenna-chamber multiple scattering power. With regard to delay, we assume that $p_0(\tau)$ and $p_{\text{scatt}}(\tau)$ are exponentially decaying, as may be expected for power in a reverberation chamber. We assume that the VNA noise power is, on average, constant and invariant of τ. Combining these assumptions with (11)–(13), we have

$$p_0(\tau,\phi) = \frac{P_0}{2\pi} C_{T,\tau_{RC}}\, e^{-\frac{\tau}{\tau_{RC}}} \tag{15}$$

$$p_{\text{scatt}}(\tau,\phi) = \frac{P_{\text{scatt}}}{2\pi} C_{T,\tau_{RC}}\, e^{-\frac{\tau}{\tau_{RC}}} \tag{16}$$

$$p_{\text{noise}}(\tau,\phi) = \frac{P_{\text{noise}}}{2\pi T} \tag{17}$$

where τ_{RC} is the chamber's decay constant and $C_{T,\tau_{RC}}$ is a normalization constant given by

$$C_{T,\tau_{RC}} = \frac{1}{\tau_{RC}\left[1 - e^{-\frac{T}{\tau_{RC}}}\right]}. \tag{18}$$

Techniques for calculating the chamber's decay constant are described in [31]. Note that, for simplicity, we have neglected the effects of windowing and aliasing. This should be acceptable provided that $T \gg \tau_{RC}$ and the measurement's temporal resolution (i.e., reciprocal of the measurement bandwidth) is much less than τ_{RC}.

B. Noise Floor Estimation and Normalization

In the following sections, we use the measurement model to estimate the noise floor of different power spectra. These noise floor estimates are then used to normalize the associated power spectra, as was done for the power profiles and spectra presented in Figs. 2–7. This noise-floor normalization facilitates comparisons between different measurements while also providing SNR-like information useful for evaluating measurement uncertainty. Note that a given power spectrum's noise floor estimate also applies to the associated power profiles. That is, we use the power-angle spectrum's noise floor estimate to normalize both the power-angle spectrum estimate (see Fig. 4) and the power-angle profiles (see Figs. 2–3).

To facilitate our noise floor normalization, we normalize the total power in the model to unity:

$$P_0 + P_{\text{scatt}} + P_{\text{noise}} = 1 \tag{19}$$

and apply an analogous normalization to the ensemble average of the measured power profiles. Specifically, we normalize each measured power-angle profile associated with a given center frequency (i.e., at nine paddle orientations and nine closely spaced frequencies) by a common factor such that

$$\int_0^{2\pi} \langle p^{(n)}(\phi)\rangle_n\, d\phi = 1 \tag{20}$$

and we normalize each measured power-delay-angle profile by a common factor such that

$$\int_0^{2\pi}\int_0^{T} \langle p^{(n)}(\tau,\phi)\rangle_n\, d\phi d\tau = 1. \tag{21}$$

1) Power-Angle Spectrum: Integrating the power-delay-angle spectrum defined by (10) and (15)–(17) with respect to delay τ, we have

$$p(\phi) = \frac{1}{2\pi}\left(P_0 + P_{\text{scatt}} + P_{\text{noise}}\right) \tag{22}$$

where the terms containing P_{scatt} and P_{noise} contribute to the noise floor of the measured power-angle spectrum. Normalizing (22) by this noise floor leads to

$$p(\phi)\left[\frac{2\pi}{P_{\text{scatt}} + P_{\text{noise}}}\right] = \frac{P_0 + P_{\text{scatt}} + P_{\text{noise}}}{P_{\text{scatt}} + P_{\text{noise}}} \tag{23}$$

where the bracketed term appearing to the left of the equal sign is the normalization that was applied to the power-angle profiles and power-angle spectra in Figs. 2–3 and Fig. 4, respectively.

2) Power-Delay-Angle Spectrum: Analogous to (23), the noise-floor-normalized power-delay-angle spectrum is given by

$$p(\tau,\phi)\left[\frac{2\pi}{P_{\text{scatt}} C_{T,\tau_{RC}}\, e^{-\frac{\tau}{\tau_{RC}}} + \frac{P_{\text{noise}}}{T}}\right] = \frac{\left(P_0 + P_{\text{scatt}}\right) C_{T,\tau_{RC}}\, e^{-\frac{\tau}{\tau_{RC}}} + \frac{P_{\text{noise}}}{T}}{P_{\text{scatt}} C_{T,\tau_{RC}}\, e^{-\frac{\tau}{\tau_{RC}}} + \frac{P_{\text{noise}}}{T}} \tag{24}$$

where the bracketed term appearing to the left of the equal sign is the normalization that was applied to the power-delay-angle profiles in Fig. 5.

3) Unstirred Power-Delay-Angle Spectrum: The unstirred channel and associated power-delay-angle spectrum are obtained by averaging N independent and identically distributed channel measurements. Denoting the unstirred channel's power-delay-angle spectrum as $p_u(\tau,\phi)$, it may be shown that

$$p_u(\tau,\phi) = \frac{p(\tau,\phi)}{N} = \frac{p_0(\tau,\phi) + p_{\text{scatt}}(\tau,\phi) + p_{\text{noise}}(\tau,\phi)}{N}. \tag{25}$$

In contrast to the power-delay-angle spectra of the individual channel measurements, for the unstirred channel, the term containing $p_0(\tau,\phi)$ is a (statistical) noise contribution associated with the variance in the ensemble average of N realizations of $h_0^{(n)}(f,\mathbf{r})$. Thereby, the noise-floor-normalized unstirred power-delay-angle spectrum is given by

$$p_u(\tau,\phi)\left[\frac{2\pi N}{\left(P_0 + P_{\text{scatt}}\right) C_{T,\tau_{RC}}\, e^{-\frac{\tau}{\tau_{RC}}} + \frac{P_{\text{noise}}}{T}}\right] = 1 \tag{26}$$

where the bracketed term appearing to the left of the equal sign is the normalization applied to the unstirred power-delay-angle profile in Fig. 7. Note that (26)'s noise-floor-normalized unstirred power-delay-angle spectrum evaluates to unity. For an

ideal, well-stirred reverberation chamber, $\langle h^{(n)}(f,\mathbf{r})\rangle_n \to 0$ as $N \to \infty$. A nonzero $\langle h^{(n)}(f,\mathbf{r})\rangle_n$ is, thus, due to a finite N, and a nonzero $p_u(\tau,\phi)$ is due to the variance in the complex average of N channel measurements. Large deviations from unity in Fig. 7 arise because the actual measured $\langle h^{(n)}(f,\mathbf{r})\rangle_n$ is non-zero due to unstirred multipath components.

4) Stirred Power-Delay-Angle Spectrum: The stirred channel and associated power-delay-angle spectrum are obtained by subtracting the unstirred channel estimate from each of the N channel measurements. Denoting the stirred channel's power-delay-angle spectrum as $p_s(\tau,\mathbf{k})$, it may be shown that

$$p_s(\tau,\phi) = \frac{N-1}{N} p(\tau,\phi) + p_u(\tau,\phi) \tag{27}$$

where $\frac{N-1}{N}$ and $p_u(\tau,\phi)$ arise due to the subtraction of the estimated mean. As in (26), $p_u(\tau,\phi)$ is considered as a noise contribution. Furthermore, as in (24), $p(\tau,\phi)$ is composed of a "signal" term $p_0(\tau,\phi)$ and "noise" terms $p_{\text{scatt}}(\tau,\phi)$ and $p_{\text{noise}}(\tau,\phi)$. Combining (26), (24), and (27), the noise-floor-normalized stirred power-delay-angle spectrum is given by

$$\begin{aligned} p_s(\tau,\phi) &\left[\frac{2\pi}{(P_0/N + P_{\text{scatt}})\, C_{T,\tau_{RC}}\, e^{-\frac{\tau}{\tau_{RC}}} + \frac{P_{\text{noise}}}{T}}\right] \\ &= \frac{(P_0 + P_{\text{scatt}})\, C_{T,\tau_{RC}}\, e^{-\frac{\tau}{\tau_{RC}}} + \frac{P_{\text{noise}}}{T}}{(P_0/N + P_{\text{scatt}})\, C_{T,\tau_{RC}}\, e^{-\frac{\tau}{\tau_{RC}}} + \frac{P_{\text{noise}}}{T}} \end{aligned} \tag{28}$$

where the bracketed term appearing to the left of the equal sign is the normalization applied to the stirred power-delay-angle profiles in Fig. 6.

Appendix B

Noise Power Estimation

Assuming the biconical antenna's radiation pattern approximates that of a z-directed infinitesimal dipole, it was shown in [6] that the biased 1-D spatial autocovariance of S_{21} measurements in a well-stirred but high-loss reverberation chamber may be modeled as (cf. [6])

$$\begin{aligned} R'_{S_{21}}(\Delta r) &= P_{\text{noise}}\delta(\Delta r) \\ &\quad + \Lambda(\Delta r/L)\left[P_0\rho_t(\Delta r) + P_{\text{scatt}}\rho_t^3(\Delta r)\right] \end{aligned} \tag{29}$$

where Δr is a linear displacement, $\rho_t(\Delta r)$ is the 1-D spatial correlation function of the transverse electric field (see [3]), L is the total scan distance plus an additional increment corresponding to the discrete scan stepsize, $\delta_0(x)$ is the Kronecker delta function, and $\Lambda(x)$ is a triangular window defined as

$$\Lambda(x) = \begin{cases} 1 - |x| & \text{for } |x| \le 1 \\ 0 & \text{otherwise.} \end{cases} \tag{30}$$

Due to the mechanics of our 2-D positioner, the additional power due to multiple scattering (i.e., P_{scatt}) depends on the scan direction (see [28]). To obtain an aggregate value of P_{scatt} for use in our noise floor estimation in Appendix A, we estimate the quantities P_0, P_{scatt}, and P_{noise} from 1-D spatial autocovariance estimates taken along the 2-D measurement region's two diagonals. The appropriate biased 1-D spatial autocovariance model for spatial autocovariance estimates calculated along the measurement region's diagonal is

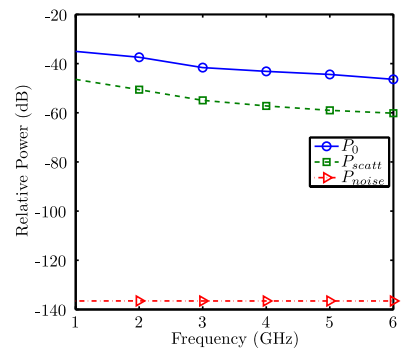

Fig. 8. Estimates of the spatial autocovariance model coefficients at the different center frequencies as obtained from a least-squares fit of the model to measured spatial autocovariances.

$$\begin{aligned} R'_{S_{21}}(\Delta r) &= P_{\text{noise}}\delta(\Delta r) \\ &\quad + \Lambda^2(\Delta r/L)\left[P_0\rho_t(\Delta r) + P_{\text{scatt}}\rho_t^3(\Delta r)\right] \end{aligned} \tag{31}$$

which accounts for the bias in the measurement region's 2-D spatial autocovariance. Note that L is now the length of the measurement region's diagonal plus an additional increment corresponding to the discrete diagonal stepsize. A fit of (31)'s model to a measured spatial autocovariance allows for the determination of the model coefficients P_0, P_{scatt}, and P_{noise}, which define the power contributed by each term.

At each of the nine center frequencies considered in Figs. 2–4, we calculated diagonal-based 1-D spatial autocovariances for measurements at each of the nine different paddle orientations and within a $9B_c$ bandwidth of the center frequency. The average of these spatial autocovariances was combined with the model presented in (31) to estimate P_0, P_{scatt}, and P_{noise} at each center frequency. As in [6], these quantities were estimated in the wavenumber domain via a least-squares fit in decibels.

Fig. 8 presents the results of this estimation procedure. The least-squares fitting procedure was not able to reliably estimate the VNA noise power P_{noise}. From auxiliary VNA noise measurements, we expect $P_{\text{noise}} < -70$ dB, which is at least 10 dB below the power due to multiple scattering. This indicates that the uncertainty in synthetic-aperture measurements in a reverberation chamber is dominated by multiple scattering power as found in [6], whereby the impact of underestimating the VNA noise is expected to be negligible.

The corresponding frequency-dependent measurement SNR, as given by

$$\text{SNR} = \frac{P_0}{P_{\text{scatt}} + P_{\text{noise}}} \tag{32}$$

is presented in Table I. For the power-angle spectrum normalization defined in (23), the frequency-dependent estimates of P_0, P_{scatt}, and P_{noise} were used directly in the normalization. For the power-delay-angle spectrum normalizations defined in (24), (26), and (28), the mean values of the frequency-dependent estimates were used.

APPENDIX C

UNCERTAINTY

For a nonzero quantity s, we may express the uncertainty in an estimate $\hat{s}$ as (cf. [25], [37])

$$u_{dB} = 10\log_{10}\left(1 \pm \frac{\sigma_{\hat{s}}}{\hat{s}}\right) \tag{33}$$

where u_{dB} is the one-sigma uncertainty in decibels, and $\sigma_{\hat{s}}$ is the standard deviation of the estimate.

A. Power Profile

For the noise-floor normalized power profile quantities presented in Sections III and V, we attribute our measurement uncertainty to a combination of VNA noise and antenna-chamber multiple scattering. We assume power contributions from the signal and noise terms are exponentially distributed whereby their standard deviations equal their means. Denoting $\hat{s}$ and $\hat{n}$ as estimates of the average signal and noise powers, respectively, an arbitrary noise-floor normalized power quantity estimate $\hat{p}/\hat{n}$ may be expressed as

$$\frac{\hat{p}}{\hat{n}} = \frac{\hat{s}+\hat{n}}{\hat{n}} \tag{34}$$

whereby

$$\frac{\hat{n}}{\hat{s}} = \left(\frac{\hat{p}}{\hat{n}} - 1\right)^{-1}. \tag{35}$$

Noting that $\hat{n} = \sigma_{\hat{s}}$, (35) may be substituted into (33) to obtain the uncertainty in Section IX's noise-floor normalized power quantities. Table II tabulates the power profile uncertainty for select values of $\hat{p}/\hat{n}$.

B. Power Spectrum

For the noise-floor normalized power-angle spectra quantities presented in Section IV, additional uncertainty arises due to averaging the signal power from N different power-angle profiles. Assuming the N power-angle profiles are independent and identically exponentially distributed, the mean-normalized relative uncertainty due to averaging is $1/\sqrt{N}$, and the combined uncertainty for the power spectra is given by the sum of squares of the uncertainties due to noise and averaging:

$$u_{dB} = 10\log_{10}\left(1 \pm \sqrt{\left[\frac{\sigma_{\hat{s}}}{\hat{s}}\right]^2 + \left[\frac{1}{\sqrt{N}}\right]^2}\right). \tag{36}$$

Table II presents the power spectra uncertainty for select values of $\hat{p}/\hat{n}$.

ACKNOWLEDGMENT

The first author thanks J. M. Ladbury of NIST for countless insightful discussions.

REFERENCES

[1] D. A. Hill, "Plane wave integral representation for fields in reverberation chambers," *IEEE Trans. Electromagn. Compat.*, vol. 40, no. 3, pp. 209–217, Aug. 1998.

[2] R. Mitra and T. F. Trost, "Statistical simulations and measurements inside a microwave reverberation chamber," in *IEEE Int. Symp. Electromagn. Compat.*, Aug. 18–22, 1997, pp. 48–53.

[3] D. A. Hill and J. M. Ladbury, "Spatial-correlation functions of fields and energy density in a reverberation chamber," *IEEE Trans. Electromagn. Compat.*, vol. 44, no. 1, pp. 95–101, Feb. 2002.

[4] P. D. Doncker and R. Meys, "Statistical response of antennas under uncorrelated plane wave spectrum illumination," *Electromagnetics*, vol. 24, no. 6, pp. 409–423, 2004.

[5] A. Khaleghi, "Diversity techniques with parallel dipole antennas: radiation pattern analysis," *Progr. Electromagnetics Res.*, vol. 64, pp. 23–42, 2006.

[6] R. J. Pirkl, "Spatial autocovariances of S-parameter measurements in a lossy reverberation chamber," *IEEE Trans. Electromagn. Compat.*, vol. 55, no. 4, pp. 671–682, 2013.

[7] T. B. Hansen, "Correlation and capacity calculations with reference antennas in an isotropic environment," *Int. J. Antennas Propag.*, vol. 2012, pp. 1–14, 2012.

[8] K. Rosengren and P.-S. Kildal, "Radiation efficiency, correlation, diversity gain and capacity of a six-monopole antenna array for a MIMO system: Theory, simulation and measurement in reverberation chamber," *IEE Proc.-Microw. Antennas Propag.*, vol. 152, no. 1, pp. 7–16, Feb. 2005.

[9] C. L. Holloway, H. A. Shah, R. J. Pirkl, W. F. Young, D. A. Hill, and J. Ladbury, "Reverberation chamber techniques for determining the radiation and total efficiency of antennas," *IEEE Trans. Antennas Propag.*, vol. 60, no. 4, pp. 1758, Apr. 2012.

[10] D. A. Hill, "Aperture excitation of electrically large, lossy cavities," *IEEE Trans. Electromagn. Compat.*, vol. 36, no. 3, pp. 169–178, Aug. 1994.

[11] U. F. Carlberg, P.-S. Kildal, A. Wolfgang, O. Sotoudeh, and C. Orlenius, "Calculated and measured absorption cross sections of lossy objects in reverberation chamber," *IEEE Trans. Electromagn. Compat.*, vol. 46, pp. 146–2004, May 2004.

[12] C. L. Holloway, D. A. Hill, M. Sandroni, J. M. Ladbury, J. S. Coder, G. Koepke, A. C. Marvin, and Y. He, "Use of reverberation chambers to determine the shielding effectiveness of physically small, electrically large enclosures and cavities," *IEEE Trans. Electromagn. Compat.*, vol. 50, no. 4, pp. 770–782, Nov. 2008.

[13] P.-S. Kildal and K. Rosengren, "Correlation and capacity of MIMO systems and mutual coupling, radiation efficiency, and diversity gain of their antennas: Simulations and measurements in a reverberation chamber," *IEEE Commun. Mag.*, vol. 42, no. 2, pp. 104–112, Dec. 2004.

[14] J. Carlsson, U. Carlberg, A. Hussain, and P.-S. Kildal, "About measurements in reverberation chamber and isotropic reference environment," in *Proc. ICECom*, Dubrovnik, Croatia, Sep. 20–23, 2010, pp. 1–4.

[15] K. Rosengren and P.-S. Kildal, "Study of distributions of modes and plane waves in reverberation chambers for the characterization of antennas in a multipath environment," *Microw. Opt. Technol. Letters*, vol. 30, no. 6, pp. 386–391, Aug. 2001.

[16] C. Orlenius, P.-S. Kildal, and G. Poilasne, "Measurements of total isotropic sensitivity and average fading sensitivity of CDMA phones in reverberation chamber," in *Proc. IEEE AP-S Int. Symp.*, vol. 1, Washington, DC, USA, Jul. 3–8, 2005, pp. 409–412.

[17] S. J. Floris, K. A. Remley, and C. L. Holloway, "Bit error rate measurements in reverberation chambers using real-time vector receivers," *IEEE Antennas Wireless Propag. Lett.*, vol. 9, pp. 619–622, 2010. Available: http://ieeexplore.ieee.org/xpl/articleDetails.jsp?arnumber=5491049.

[18] E. Genender, C. L. Holloway, K. A. Remley, J. Ladbury, and G. Koepke, "Simulating the multipath channel with a reverberation chamber: Application to bit error measurements," *IEEE Trans. Electromagn. Compat.*, vol. 52, no. 4, pp. 766–777, Nov. 2010.

[19] U. Carlberg, J. Carlsson, A. Hussain, and P.-S. Kildal, "Ray based multipath simulation tool for studying convergence and estimating ergodic capacity and diversity gain for antennas with given far-field functions," in *Proc. ICECom*, Dubrovnik, Croatia, Sep. 20–23, 2010, pp. 1–4.

[20] R. J. Pirkl and K. A. Remley, "Mimo channel capacity in 2-D and 3-D isotropic environments," *Int. J. Antennas Propag.*, vol. 2012, pp. 1–11, 2012.

[21] C. L. Holloway, D. A. Hill, J. M. Ladbury, P. F. Wilson, G. Koepke, and J. Coder, "On the use of reverberation chambers to simulate a Rician radio environment for the testing of wireless devices," *IEEE Trans. Antennas Propag.*, vol. 11, no. 11, pp. 3167–3177, Nov. 2006.

[22] R. J. Pirkl, J. M. Ladbury, and K. A. Remley, "The reverberation chamber's unstirred field: a validation of the image theory interpretation," in *Proc. Int. Symp. Electromagn. Compat.*, Long Beach, CA, USA, Aug. 14–19, 2011, pp. 670–675.

[23] L. R. Arnaut, "Operation of electromagnetic reverberation chambers with wave diffractors at relatively low frequencies," *IEEE Trans. Electromagn. Compat.*, vol. 43, no. 4, pp. 637–653, Nov. 2001.

[24] P.-S. Kildal and C. Carlsson, "Detection of a polarization imbalance in reverberation chambers and how to remove it by polarization stirring when measuring antenna efficiencies," *Microw. Opt. Technol. Lett.*, vol. 34, no. 2, pp. 145–149, July 2002.

[25] *Electromagnetic Compatibility (EMC)—Part 4-21: Testing and Measurement Techniques—Reverberation Chamber Testing Methods*, IEC Std. IEC 61 000-4-21, Rev. 2.0, 2008

[26] J. Fuhl, J.-P. Rossi, and E. Bonek, "High-resolution 3-D direction-of-arrival determination for urban mobile radio," *IEEE Trans. Antennas Propag.*, vol. 45, no. 4, pp. 672–682, Apr. 1997.

[27] J. Laurila, K. Kalliola, M. Toeltsch, K. Hugl, P. Vainikainen, and E. Bonek, "Wide-band 3-D characterization of mobile radio channels in urban environment," *IEEE Trans. Antennas Propag.*, vol. 50, no. 2, pp. 233–243, Febr. 2002.

[28] R. J. Pirkl and K. A. Remley, "Antenna-environment multiple scattering in reverberation chambers," in *IEEE AP-S*, Spokane, WA, USA, Jul. 4–8, 2011, pp. 1–4.

[29] G. D. Durgin, *Space-Time Wireless Channels*. Upper Saddle River, NJ, USA: Prentice–Hall, 2003.

[30] K. A. Remley, S. J. Floris, H. A. Shah, and C. L. Holloway, "Static and dynamic propagation channel impairments in reverberation chambers," *IEEE Trans. Electromagn. Compat.*, vol. 53, no. 3, pp. 589–599, Aug. 2011.

[31] C. L. Holloway, H. A. Shah, R. J. Pirkl, K. A. Remley, D. A. Hill, and J. M. Ladbury, "Early time behavior in reverberation chambers and its effect on the relationships between coherence bandwidth, chamber decay time, RMS delay spread, and the chamber buildup time," *IEEE Trans. Electromagn. Compat.*, vol. 54, no. 4, pp. 714–725, Aug. 2012.

[32] J. C. West, C. F. Bunting, and V. Rajamani, "Optimal plane-wave representation of random fields in a reverberation chamber," in *2011 IEEE Int. Symp. Electromagn. Compat.*, Long Beach, CA, USA, Aug. 14–19, 2011, pp. 208–213.

[33] M. Petirsch and A. J. Schwab, "Investigation of the field uniformity of a mode-stirred chamber using diffusors based on acoustic theory," *IEEE Trans. Electromagn. Compat.*, vol. 41, no. 4, pp. 446–451, Nov. 1999.

[34] K. Rosengren, P.-S. Kildal, C. Carlsson, and J. Carlsson, "Characterization of antennas for mobile and wireless terminals in reverberation chambers: improved accuracy by platform stirring," *Microw. Opt. Technol. Lett.*, vol. 30, no. 6, pp. 391–397, Sep. 2001.

[35] P.-S. K. U. Carlberg and J. Carlsson, "Numerical study of position stirring and frequency stirring in a loaded reverberation chamber," *IEEE Trans. Electromagn. Compat.*, vol. 51, no. 1, pp. 12–17, Feb. 2009.

[36] C. M. G. Cerri, V. M. Primiani, and P. Russo, "A theoretical feasibility study of a source stirring reverberation chamber," *IEEE Trans. Electromagn. Compat.*, vol. 51, no. 1, pp. 3–11, Feb. 2009.

[37] *NIS 81: Treatment of Uncertainty in EMC Measurements*, National Measurement Accreditation Service Standard 1, May 1994.

Authors, photographs and biographies not available at the time of publication.